RSC Advances

RSC Advances

www.rsc.org/advances

ROYAL SOCIETY OF CHEMISTRY

www.rsc.org/advances

Graphical absrtract

SnO$_2$@RGO composite with outstanding shielding properties pushes its promising applications in next generation building block material for EMI shielding and stealth technology.
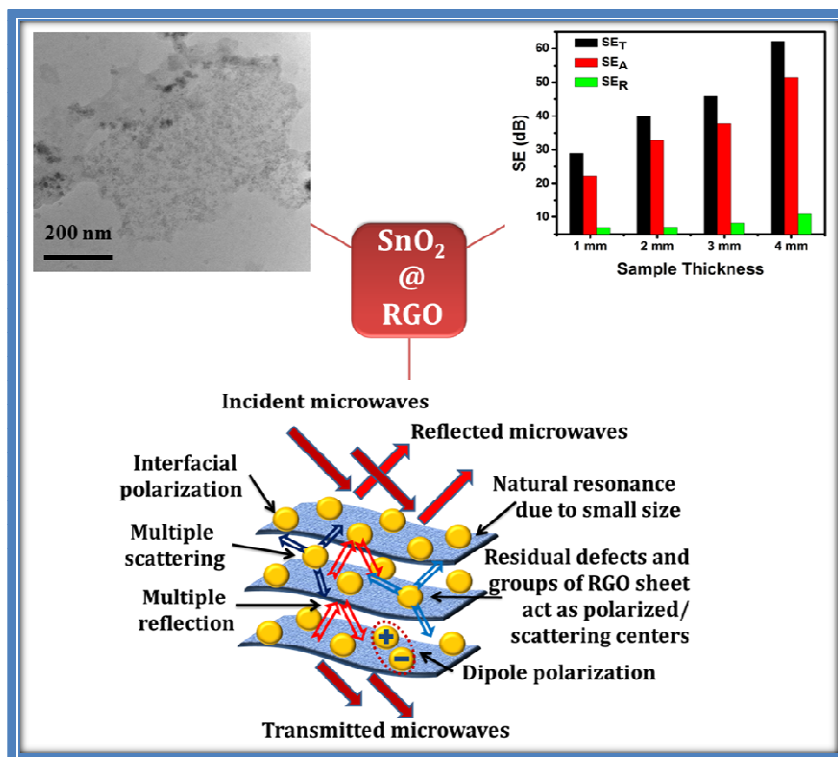
Performance of nanoarchitectured tin oxide @ reduced graphene oxide composite as a shield against electromagnetic polluting radiation

Monika Mishra[1], Avanish Pratap Singh[1], Bhanu Pratap Singh[2] and S. K. Dhawan[1]*

[1]Polymeric & Soft Materials Section, CSIR-National Physical Laboratory, Dr. K. S. Krishnan Road, New Delhi −110 012 (India)

[2]Physics and Engineering of Carbon, CSIR-National Physical Laboratory, Dr. K. S. Krishnan Road, New Delhi −110 012 (India)

Absrtract. Tin oxide nanoparticles architectured reduced graphene oxide composite (SnO_2@RGO) have been synthesised by in-situ reduction of graphene oxide in the presence of stannous chloride. Microwave shielding performance of SnO_2@RGO has been evaluated in X-band (8.2-12.4 GHz) range. XRD and TEM studies show that tin oxide nanoparticles are anchored uniformly on the surface of reduced graphene oxide sheets. A total electromagnetic interference shielding effectiveness of the order of 62 dB was achieved which is more than the required values (~30 dB) desired for techno-commercial applications.

Keywords. A.SnO_2, B. graphene, C. electromagnetic interference shielding.

* Corresponding author. Tel.: +91-11-45609401, Fax: +91-11-25726938

E-mail address: skdhawan@mail.nplindia.ernet.in

1.   Introduction

Graphene and graphene-based composites with electroconductive properties are very promising materials for numerous uses in technological applications, such as energy storage[1] , electro-optical devices[2, 3], and electromagnetic shielding[4, 5]. With the rapid growth of the electronics industry, most of the communication devices have shifted toward a higher frequency range. For abundant electrical and electronic devices, electromagnetic interference (EMI) remains a technical task in terms of the proper matching of impedance. EMI tends to reduce the response of the performance of the equipment. The shielding of various electronic devices from mobile signals and EMI is important and this is done by the microwave shielding materials[6, 7]. Most of the electromagnetic shields are ferrites[8-10], metallic magnetic materials[11-14] , and carbon nanotube (CNT) composites[15-17]. Usually, metals are used for this purpose, but the layers commonly stumble upon in metal sheets tend to cause radiation seepages, which lessen the effectiveness of the shielding material. Graphene matrix composites that contain conductive fillers are most promising EMI-shielding materials[18, 19]. Impedance matching, defect polarization relaxation and electronic dipole relaxation are present in reduced graphene oxide which all help to improve electromagnetic shielding[20]. Thus, reduced graphene oxide shows improved microwave shielding compared with graphite and carbon nanotubes, and can be likely to show better absorption than compare to high quality graphene, creating it a promising view as a microwave shielding material[21-23]. Our previous efforts based on graphene encourage us to search more and more new kind of composites with graphene[4, 24-26]. The present investigation is one of the most innovative efforts to discover new kind of material for EMI shielding.

Recent advances in architecting graphene with different materials such as Fe_3O_4[25], TiO_2[27] and gold nanoparticles[28] inspire us to design SnO_2 decorated reduced graphene oxide (RGO) sheets. RGO-SnO_2 composites have attracted significant attention recently due to their potential applications[29, 30]. The combination of the high

conductivity of the RGO sheet and tin oxide nanoparticles make it a constructive candidate for next generation microwave absorbing material. Special attention is dedicated to reducing the reinforced particle size and to allowing environmentally friendly synthesis conditions. Small, as low as 3-5 nm, average crystallite sizes have already been reported[31, 32]. Moreover, small size particles possess high anisotropy energy which also contributes in the enhancement of the microwave shielding.

In this study, we attempt to architect RGO sheets using tin oxide nanoparticles by in-situ reduction of graphene oxide in the presence of stannous chloride and hydrochloric acid, for high-performance EMI shielding application. The facile method used in this study has several advantages over the traditional GO reduction methods such as an extra reducing agent e.g. hydrazine hydrate is not required for the reduction of GO to RGO and in-situ genesis of nanoparticles leads to uniform size particles on individual RGO sheets. Such architectured SnO_2 decorated RGO sheets exhibits enhanced shielding effectiveness compared to conventional EMI shielding material. The resulting composite possesses high dielectric properties with moderate conductivity, making it a next-generation material for use in EMI shielding against electromagnetic pollution. The intended composite is promising and light-weight for practical use of EMI shielding applications in the areas of stealth technology.

2. Experimental Section

2.1 Materials

Natural graphite powder (purity 99.5%, particle size 50 μm) were procured from Loba Chemie, India, has been used to synthesize GO. Stannous (II) chloride dehydrate ($SnCl_2.2H_2O$) and $NaNO_3$, from Qualigens Fine Chemicals, India, HCl from Rankem, India, ammonia, $KmnO_4$ from Fisher scientific, India, H_2SO_4 and ethanol were obtained from Merck, India. Double distilled water of specific resistivity of 10^6 Ω-cm was used for preparing aqueous solutions and for filtration purpose.

2.2 Preparation of materials

Synthesis of tin oxide

$SnCl_2.2H_2O$ (112.81 g) was dissolved in HCl (37 wt%, 10 ml) and diluted with distilled water (500 ml) to give a $SnCl_2$–HCl solution. In order to form a uniform solution and maintaining pH approximately 10, a certain amount of ammonia (25%) was added under controlled rate (0.01-0.1 ml/min) to the $SnCl_2.HCl$ solution with vigorous stirring. The resulting solution was then stirred at 90 ^{0}C for 6 h. The precipitate obtained was separated by centrifugation and washed with distilled water to remove excess chloride ions. The resulting product was dried in a vacuum oven at 110 ^{0}C for 24 h and followed by calcination (at 400 ^{0}C for 5h in N_2 atmosphere) for improving of crystallity of SnO_2[31].

Synthesis of SnO₂ decorated RGO sheets

The chemical reduction of graphene oxide (GO) was carried out in the presence of $SnCl_2$ to fabricate SnO_2 decorated RGO. Prior to this, GO has been synthesised. The detailed method of GO synthesis was discussed in our earlier report[24]. In brief commercially available graphite powder (5 g) and $NaNO_3$ (5 g) is mixed into concentrated H_2SO_4 (230 ml). $KMnO_4$ (40 g) is added gradually with stirring and cooling, so that the temperature of the mixture is not allowed to reach beyond 20 °C. The mixture is then stirred at 35 °C for 2 h, and deionized water (200 ml) is added. The reaction is stirred for 1 hour by the addition of a large amount of deionized water (300 ml) and 30% H_2O_2 solution (30 ml), causing violent effervescence and an increase in temperature to 100°C, after which the color of the suspension changes to bright yellow. The suspension is washed with HCl solution in order to remove metal ions. The paste collected is dried at 60 °C. 2 gm of GO powder is dispersed in 500ml distilled water followed by stirring and ultrasonication for 1 h for making GO solution.

A typical preparation process for SnO_2 decorated RGO is as follows: 14 gm of $SnCl_2.2H_2O$ was added to 500ml HCl solution (100ml/l of 37wt% HCl). Then, this solution was mixed with GO solution and sonicated for 1 h. The resulting mixture was stirred for 6 h at 90 ^{0}C. The SnO_2@RGO were collected after several washing with water through centrifugation, then dried in a vacuum oven at 100 ^{0}C. Now calcination

(400 ^{0}C for 5h in N_2 atmosphere) was carried out for improvement of crystallity of SnO_2[31]. The possible reaction mechanism can be written as follow:

$$SnCl_2.2H_2O + GO + H_2O + 2HCl \rightarrow SnO_2@RGO$$

Schematic representation of RGO decoration using SnO_2 nanoparticles is shown in Figure 1 a.

2.3 Materials Characterization

The morphology of RGO/SnO_2 composites was characterized by transmission electron microscope (TECNAI G^2T30, u−TWIN) at an acceleration voltage 300.0 kV. X-ray diffraction (XRD) measurements were performed on D8 Advance XRD (Bruker) using CuKα radiation (λ = 1.54Å) in the scattering range (2θ) of 10°-80° with a scan rate of 0.02°/sec and slit width of 0.1mm. FTIR spectra were recorded on Nicolet 5700 in transmission mode in the wave number range 400-2000 cm^{-1}. The spectroscopic grade KBr pellets were used for collecting the spectra with a resolution of 4 cm^{-1} performing 32 scans. Raman analysis was carried out using Renishaw in Via Reflex spectrometer, UK with an excitation source of 514.5 nm. The resolution of the instrument was less than 1.0 cm^{-1}. The dc electrical conductivity has been measured by a standard four-probe technique, in order to eliminate contact resistance effects, using Keithley programmable current source (model 6221) and nano voltmeter (model 2182A). Electromagnetic shielding and dielectric measurements have been carried out using Agilent E8362B Vector Network Analyzer in the 8.2−12.4 GHz (X−band) microwave range. The composite has compacted in a piston cylinder assembly at 60MPa for 5 min into different thickness rectangle pellet with a dimension to fit the waveguide dimensions.

3. RESULTS AND DISCUSSION

3.1 Morphological Analysis

Figure 1 b & c demonstrates the transmission electron microscopy (TEM) images of SnO_2 nanoparticles and SnO_2 decorated RGO. Figure 1 b shows SnO_2 nanoparticles at different magnifications. Higher magnification images (Figure 1 b1 &

b2) confirm that all particles are of 3-5 nm diameter. It is evident RGO sheet was uniformly decorated by a large quantity of SnO_2 nanoparticles and the outline of both RGO and SnO_2 nanoparticles can be clearly seen as depicted in Figure 1 c. Higher magnification images (Figure 1 c2 & c3) revealed that the SnO_2 nanoparticles have grown on the surface of RGO sheet and were distributed over the RGO's surface. SnO_2 nanoparticles can exist densely on both sides of these sheets. Most importantly, there are no vacant areas of the RGO sheets that are not decorated with SnO_2 nanoparticles. It's worthy to notice that these SnO_2 nanoparticles are strongly attached with RGO sheets, because the sonication was applied during the preparation of TEM samples, indicating excellent bonding between RGO and SnO_2 nanoparticles. The presence of dielectric nanoparticles on conducting surface is helpful for enhancing the shielding of the electromagnetic wave.
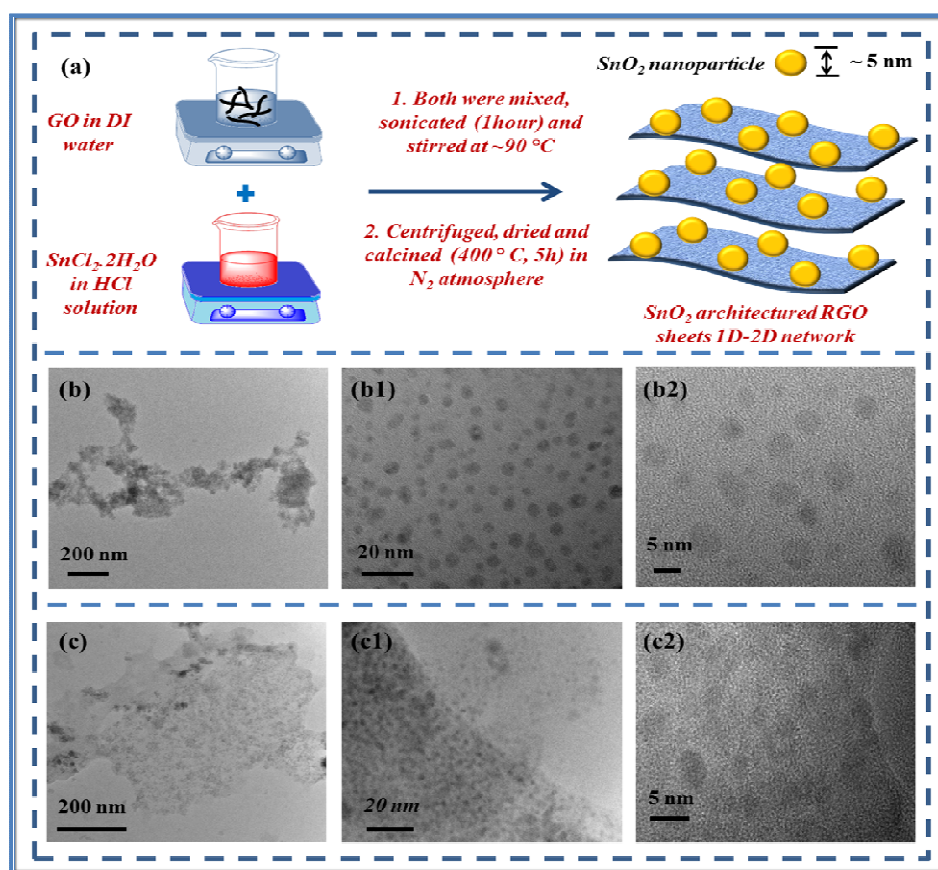
Figure 1. (a) Schematic representation of architecturing SnO_2 nanoparticles on the surface of RGO sheets, (b) TEM image of SnO_2 nanoparticles at different magnifications and (c) TEM image of as-synthesized SnO_2@RGO composite.

3.2 Structural Analysis

The crystal structure of GO, RGO and RGO-SnO_2 was characterized by XRD and the results are displayed in Figure 2a. The powder x-ray diffraction pattern of GO shows a diffraction peak around 10.2°, which corresponds to the (002) reflection of stacked GO sheets. It shows an interlayer spacing of 0.86 nm for GO which is more than graphite with an interlayer spacing of 0.34 nm. It is due to the introduction of oxygen containing groups on the GO sheets. Chemical reduction of GO to RGO leads to broadening and shifting of the XRD peak to around 24.9° corresponding to an interlayer spacing of about 0.36 nm. This is indicating the presence of residual oxygenated groups on the RGO sheets. For SnO_2@RGO, there is no diffraction peaks of GO indicating the reduction of GO to RGO by the stannous ions. The diffraction patterns and relative intensities of synthesized SnO_2 matched well with standard SnO_2 (JCPDS 41-1445), demonstrating that the nanoparticles were SnO_2 and shows that the diffraction peaks of crystalline SnO_2 nanoparticles are clearly distinguishable. It could be indexed to the tetragonal SnO_2 phase (JCPDS 41-1445). The XRD peaks of composite appearing at about 2θ = 26.5, 33.9, 51.6 can be indexed to the diffraction planes of SnO_2 (110), (101), and (211) respectively. The mean particle size (D) of the SnO_2 nanoparticles was calculated by applying the Scherrer equation to the (110) plane diffraction peak and found to be 3–5 nm in the SnO_2@RGO composite.

3.3 FTIR spectroscopy

Figure 2 b shows the FTIR spectra of GO and SnO_2@RGO. The FT-IR spectra of GO confirmed the presence of oxygen-containing groups, such as C–OH at 3420 cm^{-1}, C–O–C at 1220 cm^{-1}, and C=O in carboxylic acid moieties at 1709 cm^{-1}. Other characteristic vibrations were the O–H deformation peak at 1405 cm^{-1} and the C–O stretching peak at 1043 cm^{-1}. The peak at 1623 cm^{-1} was assigned to the contributions from the skeletal vibrations of the graphitic domains. For the SnO_2@RGO, the carboxylic acid vibration band at 1709 cm^{-1} disappeared. A weak signal for the C–OH stretching vibration at 3412 cm^{-1} could be ascribed to the vibrations of the adsorbed water molecules which is assigned to the Eu mode of SnO_2 (anti-symmetric O–Sn–O

stretching). The presence of the Eu mode (a band located at 612 cm^{-1}) in SnO$_2$@RGO indicates the incorporation of SnO$_2$ particles on the RGO sheets. Additionally, the spectrum of the SnO$_2$@RGO composite shows an absorption band at 1592 cm^{-1} (C=C stretching), indicating the restoration of the graphene network on reduction. So it could be concluded that GO was reduced by the stannous ions.
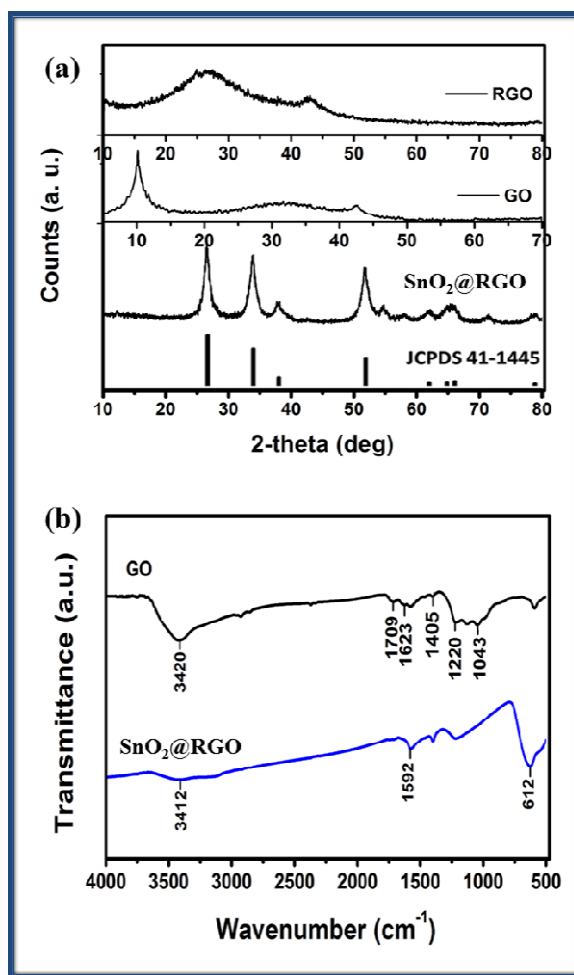
Figure 2. (a) X−ray diffraction patterns of SnO$_2$@RGO, GO and RGO (b) comparison of FTIR spectra of GO and SnO$_2$@RGO composite.

3.4 Raman spectroscopy

Raman spectroscopy is a very powerful tool for investigating the proper interaction or bonding between two components[33]. To elucidate the graphitic structure of GO, RGO and interaction among RGO, SnO$_2$ nanoparticles, Raman spectroscopy was conducted in a spectral range of 100-3300 cm^{-1}. Figure 3

shows the Raman spectra of GO, RGO, and SnO$_2$@RGO composite. The Raman spectra of GO and RGO consist of three prominent characteristic peaks, namely the D band (disorder-induced band), the G band (the tangential mode of graphitic structure), and the G' (or 2D) band. The G and D bands are due to the doubly degenerate zone centre E$_{2g}$ mode (~1580-1600) and the breathing modes of six atom rings which appears at ~ 1350 cm^{-1} due to the presence of defects in the graphite, respectively[34]. In the Raman spectrum of RGO, the D, G and 2D peak position values confirm the formation of RGO. Raman spectrum of pure SnO$_2$ nanoparticles reveals all the characteristic bands of SnO$_2$ in the low frequency region, i.e., 436, 479 (Eg), 564 (S1), 633 (A$_{1g}$)[35]. All these peaks are suppressed in the SnO$_2$@RGO composite because of the highly intense graphitic peaks present in RGO sheets. Furthermore the interaction between RGO and SnO$_2$ nanoparticles are clearly seen by the red shift in peaks of RGO from 1365 to 1353 cm^{-1} in D band and 1600 to 1593 cm^{-1} in G band. Slight shifting in the bands is an evidence of interaction between these components. Additionally, slight shift is also observed in G' band. I$_D$/I$_G$ value of SnO$_2$@RGO is higher (1.22) than RGO (1.02). It also suggests the interaction of SnO$_2$ into RGO sheet because at the time of synthesis of the SnO$_2$@RGO, SnO$_2$ interacts on the available defect sites of RGO sheet or on further occurrence of defect sites at the time of architecturing SnO$_2$ nanoparticles on RGO surface.
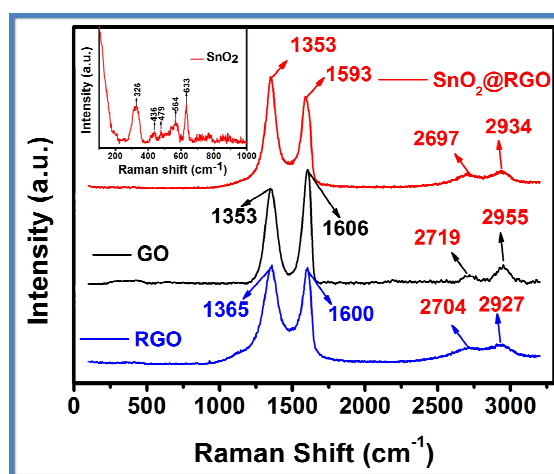
Figure 3. Raman spectra of RGO, GO, SnO$_2$ decorated RGO sheets and Inset image shows the Raman spectum of SnO$_2$ nanoparticles

3.5 Shielding Effectiveness Measurement

EMI SE of any material is the sum of the contributions of the absorption (SE$_A$), reflection (SE$_R$) and multiple reflections (SE$_M$) of the EM energy[36-38]:

$$SE = -10\log\left({P_T}/{P_I}\right) = SE_R + SE_A + SE_M$$
(1)

where, P_I and P_T are the power of incident and transmitted EM waves, respectively. According to Schelkunoff's theory, SE$_M$ can be ignored in all practical application where the shield is thicker than the skin depth (δ). For a material, the skin depth (δ) is the distance up to which the intensity of the EM wave decreases to 1/e of its original strength. The δ is related to angular frequency, relative permeability and total conductivity

$$\sigma_T = (\sigma_{dc} + \sigma_{ac})$$
(2)

Figure 4 (a-d) shows the variation of the SE with frequency in the 8.2-12.4 GHz range. From Figure 4 (a), the values of SE for SnO$_2$@RGO composite (45.8 dB) is significantly higher than both RGO (32.5 dB) and SnO$_2$ (14.2 dB) at a critical thickness of 3 mm. It proposed that the addition of dielectric filler enhances the SE of RGO. Therefore, SnO$_2$@RGO is better option compare to SnO$_2$ and RGO composite independently. We also explored the effect of varying thickness of the composites on the EMI shielding performances. For this rectangular pallets of different thicknesses (1.0 mm, 2.0 mm, 3.0 mm and 4.0 mm, respectively) were placed in the X-band sample holder and SE is measured in frequency range of 8.2-12.4 GHz. The plot of microwave SE versus frequency for SnO$_2$@RGO having four different thicknesses are shown in Figure 4 b The value of SE$_T$ is 29 dB for sample having thickness of 1 mm and it reaches to 62 dB for 4.0 mm thick sample.

The term SE$_R$ and SE$_A$ can be defined as[25, 38]:

$$SE_R = -10\log(1-R)$$
(3)

$$SE_A = -10\log(1-A_{eff}) = -10\log(T/1-R).$$
(4)

Therefore, the effective absorbance (A_{eff}) can be described as with respect to the power of the effectively incident EM wave inside the shielding material.

$$A_{eff} = (1 - R - T)/(1 - R) \tag{5}$$

In terms of dielectric losses the SE_A can also be written as[25]

$$SE_A(dB) = 20d\sqrt{\frac{\mu\omega^2\varepsilon_o\varepsilon''}{2}}.\log e \tag{6}$$

In terms of tan delta the above equation can be written as

$$SE_A(dB) = 20d\sqrt{\frac{\mu\omega^2\varepsilon_o\varepsilon'\tan\text{delta}}{2}}.\log e \tag{7}$$

i.e. SE_A is directly proportional to tan delta.

The as calculated SE_A and SE_R from experimental scattering parameters (S_{11}, S_{22}, S_{12}, S_{21}) are plotted in Figure 4(c). The values of SE_A for SnO_2@RGO composite are considerably increases with increase in thickness over the entire frequency range. The SE_A values of the composite with 1, 2, 3 and 4 mm thickness are in the range of 22.58-23.15, 29.19-35.90, 37.80-42.09 and 45.39-80.14 respectively. On the other hand the values of SE_R are very low as compared to SE_A. Moreover, the change in SE_R is very small with increase of thickness. Therefore, for SnO_2@RGO composite, the mechanism of shielding is mainly absorption of EM waves due to highly conductive composite and the absorption is proportional to the thickness of the composite material. Figure 4d shows the overall changes in % attenuation with thickness in which changes in reflection loss with increasing the thickness is very small compared to absorption. According to shielding theory, SE_A becomes more dominant as compared to the SE_R in the microwave range. This may be caused by the shallow skin depth and high conductivity (σ_{ac}) values at such high frequencies[39, 40] Although electrical conductivity of SnO_2@RGO is high (13.74 S/cm) but it is much smaller than that of graphene reported theoretically. This is because the inter transport of charge carriers in SnO_2@RGO is a complex phenomenon of electron tunneling and hopping and is different from single layer of

graphene[5, 25, 38, 41-43]. Furthermore, conductivity of SnO_2@RGO composite is acceptable because insulating SnO_2 particles hinders the free flow of electrons in the SnO_2@RGO composite.

The observed high shielding effectiveness could be explained in terms of dielectric losses. According to, the EM theory, dielectric losses are the result of complex phenomena like natural resonance, dipole relaxation, electronic polarization and its relaxation and certainly the unique structure of the shield. When the frequency of the applied field is increased, the electrons present in the system cannot reorient themselves fast enough to respond to applied electric field, and improves dielectric constant. SnO_2 nanoparticles anchored on the top surface of RGO sheets act as polarized center and improves polarization which results in more microwave shielding. High electrical conductivity of SnO_2@RGO also enhances the shielding properties. SnO_2 nanoparticles act as tiny dipoles which get polarized in the presence of EM field and result in better microwave shielding.

Figure 4 c curves exhibits broad multi peaks which imply the presence of natural resonance caused by the enhanced surface anisotropy of the small size of SnO_2 particles. Anisotropy energy of the small size materials,[44] especially in the nanoscale, would be higher due to surface anisotropic field due to the small size effect.[45] The higher anisotropy energy also contributes in the enhancement of the microwave shielding. Interfacial polarization occurs in heterogeneous media due to accumulation of charges at the interfaces, formation of dipoles. Interfaces among tin oxide nanoparticles and RGO sheets further contribute to dielectric losses.
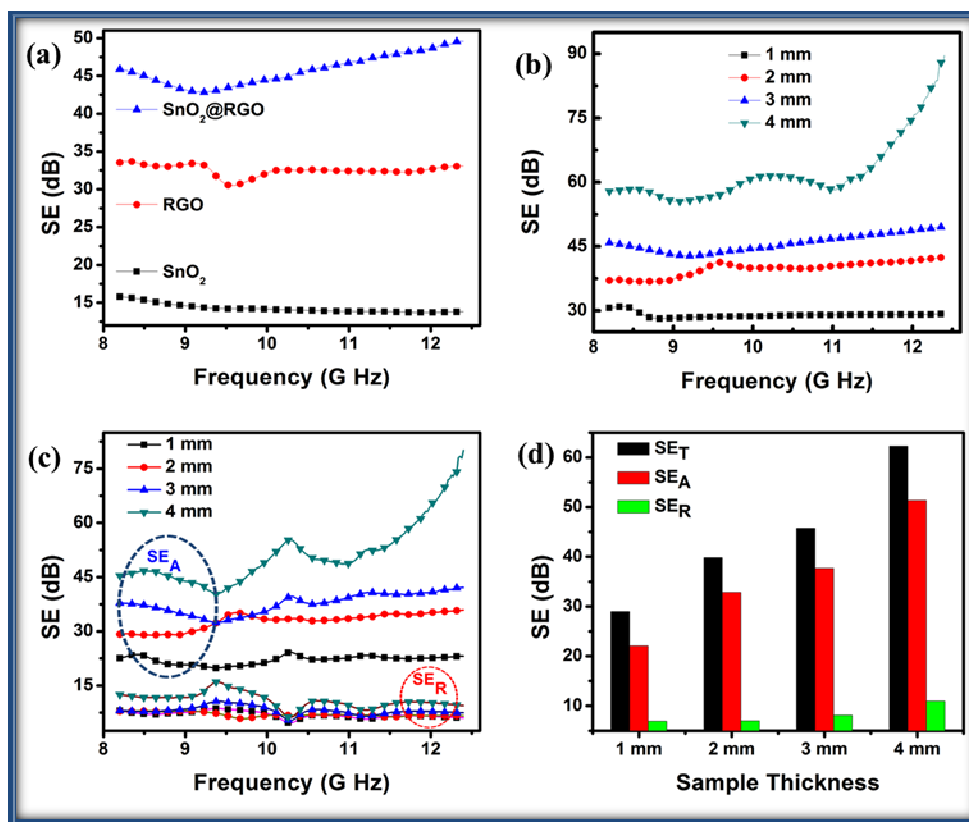
Figure 4. (a) Variation in EMI shielding effectiveness SE_T of SnO_2, RGO and SnO_2@RGO composite at a critical thickness of 3 mm, (b) Behavior of SE_T for SnO_2@RGO composite at different thicknesses (c) behavior of SE_A and SE_R with frequency for different thicknesses of SnO_2@RGO composite and (d) SE_T, SE_A and SE_R for different thicknesses of SnO_2@RGO composite.

From these results, we conclude that the filling of SnO_2 nanoparticles exhibit better microwave shielding properties in comparison with pristine SnO_2 nanoparticles, pure RGO, γ-Fe_2O_3 nanoparticles and RGO/iron oxide composite, MnO_2 decorated graphene nanoribbion reported earlier[46, 47].
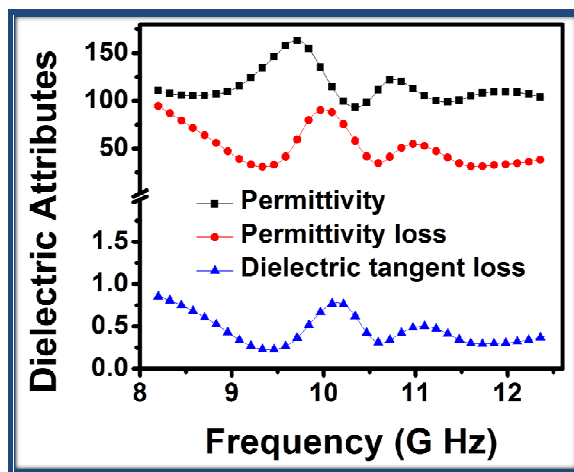
Figure 5. Frequency dependence of the permittivity, permittivity loss and dielectric tangent loss of SnO_2@RGO composite.

Dielectric permittivities were also investigated in order to understand the microwave shielding properties and dielectric loss mechanism of SnO_2@RGO composite in detail. Figure 5 shows the permittivity (ε'), permittivity loss (ε'') and tangent loss (tan δ = $\varepsilon''/\varepsilon'$) as a function of frequency for SnO_2@RGO composite at a thickness of 3 mm. The permittivity symbolizes the intensity of polarization or the electrical energy storage ability of a material. and permittivity loss represents the energy loss during the activation by an EM wave. The highest value of ε' was observed 160 at 9.6 GHz. The value of ε'' is lower than ε' and it fluctuates from 94 to 32 in 8.2 to 12.4 GHz. The values of dielectric tangent loss were observed in the range 0.85 to 0.36. The high value of ε'' and tan δ for SnO_2@RGO composite exhibit high dielectric losses. Interestingly, there are two humps observed in dielectric tangent loss which proposed that the two main phenomena's are responsible for dielectric losses. These may be interfacial polarization between SnO_2 nanoparticles and RGO sheets and effective anisotropy energy of the SnO_2@RGO composite. In the effective anisotropy energy, the parallel (RGO sheets are in a plane) and random alignment of RGO sheets is of particular importance. According to the physics principal's, the polarization intensity is directly proportional to the displacement of positive and negative charges during the activation by an EM

wave. When EM waves incident perpendicular to the RGO plane, the effective anisotropy energy is higher as polarization intensity is higher in the plane direction. Therefore contribution to the total EMI SE is higher when EM wave incident perpendicular to RGO plane, as compared to when EM wave incident parallel to RGO plane[5]. Furthermore the existence of residual defects/groups in RGO sheet[48] and multiple reflections with in the shield enhances the microwave shielding ability of the composites. To further give a visual demonstration of the microwave shielding mechanism as discussed above a schematic is given in Figure 6. From all the above, the results of SnO_2@RGO composite illustrates that such structure could be potentially used as microwave shielding material.
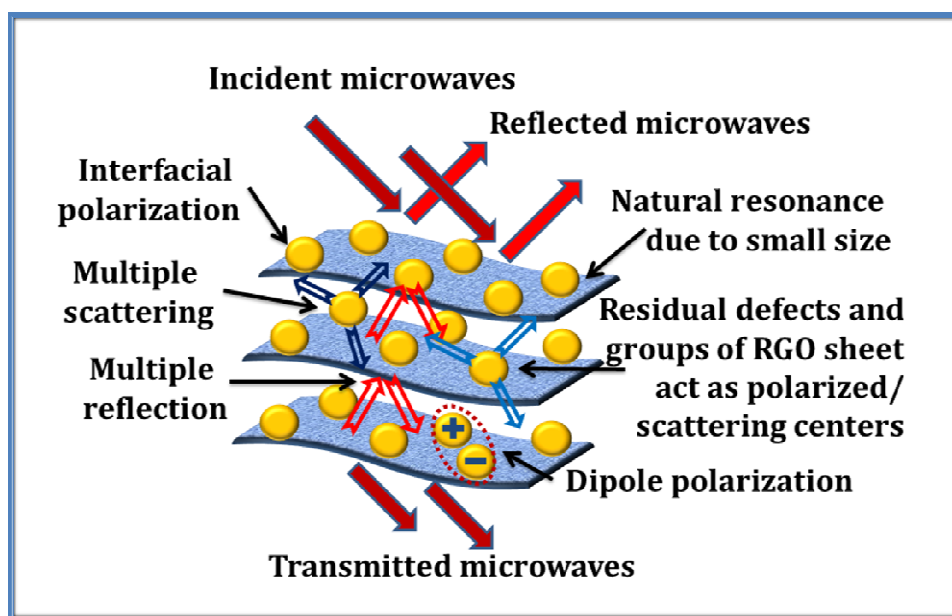
Figure 6. Schematic presentation of possible microwave shielding mechanisms in the SnO_2@RGO composite.

4. Conclusions

In summary, we have successfully designed high performance tin oxide nanoparticles decorated RGO for suppressing electromagnetic pollution. Presence of

dielectric filler SnO_2 nanoparticles on RGO sheets enhances the dielectric losses which can be attributed to natural resonance, dipole relaxation, electronic polarization related relaxation, interfacial polarization and the effective anisotropy energy. Moreover, this unique SnO_2@RGO composite contributes to more scattering and leads to the high shielding effectiveness (SE_T~62dB at a thickness of 4mm) as compared to conventional materials. This ingenious light weight nanocomposite with outstanding shielding properties pushes its promising applications in next generation building block material for EMI shielding and stealth technology.

References

1. Z.-S. Wu, G. Zhou, L.-C. Yin, W. Ren, F. Li and H.-M. Cheng, *Nano Energy*, 2012, **1**, 107-131.
2. X. Wang, L. Zhi and K. Mullen, *Nano Letters*, 2007, **8**, 323-327.
3. M. Liu, X. Yin, E. Ulin-Avila, B. Geng, T. Zentgraf, L. Ju, F. Wang and X. Zhang, *Nature*, 2011, **474**, 64-67.
4. A. P. Singh, M. Mishra, P. Sambyal, B. K. Gupta, B. P. Singh, A. Chandra and S. K. Dhawan, *Journal of Materials Chemistry A*, 2013.
5. N. Yousefi, X. Sun, X. Lin, X. Shen, J. Jia, B. Zhang, B. Tang, M. Chan and J.-K. Kim, *Advanced Materials*, 2014, n/a-n/a.
6. T. Xia, C. Zhang, N. A. Oyler and X. Chen, *Advanced Materials*, 2013, **25**, 6905-6910.

7. X. C. Tong, *Advanced Materials and Design for Electromagnetic Interference Shielding*, Taylor & Francis2008.

8. E. A. Maguire and D. W. Readey, *Journal of the American Ceramic Society*, 1976, **59**, 434-437.

9. W. Li, X. Qiao, H. Zhao, S. Wang and Q. Ren, *Journal of Nanoscience and Nanotechnology*, 2013, **13**, 793-798.

10. K. Khan, *J Supercond Nov Magn*, 2014, **27**, 453-461.

11. W. Xie, H. Cheng, Z. Chu, Y. Zhou, G. Tang and Y. Xu, *J. Wuhan Univ. Technol.-Mat. Sci. Edit.*, 2007, **22**, 218-220.

12. M. Matsumoto and Y. Miyata, *Magnetics, IEEE Transactions on*, 1997, **33**, 4459-4464.

13. V. M. Petrov and V. V. Gagulin, *Inorganic Materials*, 2001, **37**, 93-98.

14. E. J. Borchers, C. E. Boyer, C. D. Hoyle and R. J. Kuo, Google Patents1992.

15. A. P. Singh, B. K. Gupta, M. Mishra, Govind, A. Chandra, R. B. Mathur and S. K. Dhawan, *Carbon*, 2013, **56**, 86–96.

16. A. Saib, L. Bednarz, R. Daussin, C. Bailly, L. Xudong, J. Thomassin, C. Pagnoulle, C. Detrembleur, R. Jerome and I. Huynen, *Microwave Theory and Techniques, IEEE Transactions on*, 2006, **54**, 2745-2754.

17. J.-M. Thomassin, X. Lou, C. Pagnoulle, A. Saib, L. Bednarz, I. Huynen, R. Jérôme and C. Detrembleur, *The Journal of Physical Chemistry C*, 2007, **111**, 11186-11192.

18. H.-B. Zhang, Q. Yan, W.-G. Zheng, Z. He and Z.-Z. Yu, *ACS Applied Materials & Interfaces*, 2011, **3**, 918-924.

19. X. Bai, Y. Zhai and Y. Zhang, *The Journal of Physical Chemistry C*, 2011, **115**, 11673-11677.

20. C. Wang, X. Han, P. Xu, X. Zhang, Y. Du, S. Hu, J. Wang and X. Wang, *Applied Physics Letters*, 2011, **98**, 072906-072903.

21. W. Choi and J. Lee, *Graphene: Synthesis and Applications*, Taylor & Francis2011.

22. H. Seul Ki, K. Ki Yeong, K. Taek Yong, K. Jong Hoon, P. Seong Wook, K. Joung Ho and C. Byung Jin, *Nanotechnology*, 2012, **23**, 455704.

23. R. Murali, *Graphene Nanoelectronics: From Materials to Circuits*, Springer2011.

24. M. Mishra, A. P. Singh and S. K. Dhawan, *Journal of Alloys and Compounds*, 2013, **557**, 244-251.

25. A. P. Singh, P. Garg, F. Alam, K. Singh, R. B. Mathur, R. P. Tandon, A. Chandra and S. K. Dhawan, *Carbon*, 2012, **50**, 3868–3875.

26. P. Sambyal, A. P. Singh, M. Verma, M. Farukh, B. P. Singh and S. K. Dhawan, *RSC Advances*, 2014, **4**, 12614-12624.

27. X.-Y. Zhang, H.-P. Li, X.-L. Cui and Y. Lin, *Journal of Materials Chemistry*, 2010, **20**, 2801-2806.

28. Z. Xiong, L. L. Zhang, J. Ma and X. S. Zhao, *Chemical Communications*, 2010, **46**, 6099-6101.

29. S. Humaira, K. C. Kemp, C. Vimlesh and S. K. Kwang, *Nanotechnology*, 2012, **23**, 355705.

30. X. Zhu, Y. Zhu, S. Murali, M. D. Stoller and R. S. Ruoff, *Journal of Power Sources*, 2011, **196**, 6473-6477.

31. J. Zhang, Z. Xiong and X. S. Zhao, *Journal of Materials Chemistry*, 2011, **21**, 3634-3640.

32. S. Sladkevich, J. Gun, P. V. Prikhodchenko, V. Gutkin, A. A. Mikhaylov, V. M. Novotortsev, J. X. Zhu, D. Yang, H. H. Hng, Y. Y. Tay, Z. Tsakadze and O. Lev, *Nanotechnology*, 2012, **23**, 485601.

33. T. K.Gupta, B. P.Singh, S. R.Dhakate, V. N. Singh and R. B. Mathur, *Journal of Materials Chemistry A*, 2013.

34. A. C. Ferrari, J. C. Meyer, V. Scardaci, C. Casiraghi, M. Lazzeri, F. Mauri, S. Piscanec, D. Jiang, K. S. Novoselov, S. Roth and A. K. Geim, *Physical Review Letters*, 2006, **97**, 187401.

35. A. Diéguez, A. Romano-Rodríguez, A. Vilà and J. R. Morante, *Journal of Applied Physics*, 2001, **90**, 1550-1557.

36. A. M. Nicolson and G. F. Ross, *IEEE Trans. Instrum Mea*, 1970, **19** 377−382.

37. W. B. Weir, *Proc IEEE*, 1974, **62**, 33−36.

38. B. Wen, X. X. Wang, W. Q. Cao, H. L. Shi, M. M. Lu, G. Wang, H. B. Jin, W. Z. Wang, J. Yuan and M. S. Cao, *Nanoscale*, 2014.

39. N. C. Das, D. Das, T. K. Khastgir and A. C. Chakrraborthy, *Composites A.*, 2000, **31**, 1069-1081.

40. N. F. Colaneri and L. W. Shacklette, *IEEE Trans. Instrum. Meas.*, 1992, **41**, 29.

41. C. Gómez-Navarro, R. T. Weitz, A. M. Bittner, M. Scolari, A. Mews, M. Burghard and K. Kern, *Nano Letters*, 2007, **7**, 3499-3503.

42. S. R. Pathipati, E. Pavlica, E. Treossi, R. Rizzoli, G. P. Veronese, V. Palermo, L. Chen, D. Beljonne, J. Cai and R. Fasel, *Organic Electronics*, 2013, **14**, 1787-1792.

43. P. Lian, X. Zhu, S. Liang, Z. Li, W. Yang and H. Wang, *Electrochimica Acta*, 2011, **56**, 4532-4539.

44. D. L. Leslie-Pelecky and R. D. Rieke, *Chem. Mater.*, 1996, **8**, 1770-1783.

45. Y.-J. Chen, P. Gao, R.-X. Wang, C.-L. Zhu, L.-J. Wang, M.-S. Cao and H.-B. Jin, *J. Phys. Chem. C*, 2009, **113**, 10061–10064.

46. K. Singh, A. Ohlan, V. H. Pham, B. R, S. Varshney, J. Jang, S. H. Hur, W. M. Choi, M. Kumar, S. K. Dhawan, B.-S. Kong and J. S. Chung, *Nanoscale*, 2013, **5**, 2411-2420.

47. T. K. Gupta, B. P. Singh, V. N. Singh, S. Teotia, A. P. Singh, I. Elizabeth, S. R. Dhakate, S. K. Dhawan and R. B. Mathur, *Journal of Materials Chemistry A*, 2013.

48. X. Sun, J. He, G. Li, J. Tang, T. Wang, Y. Guo and H. Xue, *J. Mater. Chem. C*, 2013, **1**, 765-777.